JM PAPERS

CrossMark

On the turbulence dynamics induced by a surrogate seagrass canopy

Robert C. Houseago[1], Liu Hong[2], Shyuan Cheng[2], James L. Best[2,3,4,5], Daniel R. Parsons[1] and Leonardo P. Chamorro[2,3,5,6],†

[1]Energy and Environment Inst. University of Hull, Cottingham Road, Hull HU6 7RX, UK

[2]Mechanical Science and Engineering, University of Illinois, Urbana, IL 61801, USA

[3]Geology, University of Illinois, Urbana, IL 61801, USA

[4]Geography and GIS, University of Illinois, Urbana, IL 61801, USA

[5]Civil and Environmental Engineering, University of Illinois, Urbana, IL 61801, USA

[6]Aerospace Engineering, University of Illinois, Urbana, IL 61801, USA

The distinct turbulence dynamics and transport modulated by a common seagrass species were investigated experimentally using a flexible surrogate canopy in a refractive-index-matching environment that enabled full optical access. The surrogate seagrass replicated the dynamic behaviour and morphological properties of its natural counterpart. The flows studied were subcritical with Froude numbers $Fr < 0.26$ and concerned five Reynolds numbers $Re \in [3.4 \times 10^4, 1.1 \times 10^5]$ and Cauchy numbers $Ca \in [120, 1200]$. Complementary rigid canopy experiments were also included to aid comparative insight. The flow was quantified in wall-normal planes in a developed region using high-frame-rate particle image velocimetry. Results show that the deflection and coordinated waving motion of the blades redistributed the Reynolds stresses above and below the canopy top. Critically, in-canopy turbulence associated with the seagrass lacked periodic stem wake vortex shedding present in the rigid canopy, yet the flexible canopy induced vortex shedding from the blade tips. Inspection of spatial and temporal characteristics of coherent flow structures using spectral proper orthogonal decomposition reveals that Kelvin–Helmholtz-type vortices are the dominant flow structures associated with the waving motion of the seagrass and that modulated the local flow exchange in both rigid and flexible canopies. A barrier-like effect produced by the blade deflections blocked large-scale turbulence transport, thereby reducing vortex penetration into the canopy. In addition, we uncovered a transition from sweep-dominated to ejection-dominated behaviour in the surrogate seagrass. We hypothesise that the vortices created during the upward blade motion period play a major role in the

† Email address for correspondence: lpchamo@illinois.edu

sweep-to-ejection-dominated transition. Conditionally averaged quadrant analysis on the downward and upward blade motion supports this contention.

Key words: river dynamics, channel flow, hydraulics

1. Introduction

Aquatic vegetation, or macrophytes, modulate the spatial and temporal hydrodynamics within riverine and coastal environments. Vegetation regulates turbulence and mixing processes, which, in turn, control ecological and morphological system functions (Waycott *et al.* 2009; Nepf 2012). Associated flow alterations can reduce sediment transport and erosion rates, support nature-based protection of riverbeds and coastlines (Luhar, Rominger & Nepf 2008; Christianen *et al.* 2013; Luhar & Nepf 2013) and influence the broad-scale morphodynamics (Cotton *et al.* 2006; Vacchi *et al.* 2017). Turbulent fluxes and particulate exchange between canopies and free-stream flow are intrinsic to nutrient mixing, providing favourable conditions that support biodiversity (Edgar 1990; Clarke 2002) along with altering carbon capture (Prentice *et al.* 2019). The various benefits of submerged vegetation as natural ecosystems have motivated the characterisation and quantification of canopy-induced turbulence dynamics across scales.

The in-canopy flow, canopy shear layer and coherent vortices and the penetration of turbulence into the canopy all contribute to the vertical mass transfer of dissolved species (nutrients) (Lowe *et al.* 2005; Falter *et al.* 2007). These processes are modulated by canopy morphology and density, which are increasingly complex in flexible canopies due to the blade motions (Weitzman *et al.* 2013). Weitzman *et al.* (2015) noted that the presence of biomass in the lower canopy region promotes the velocity attenuation within a canopy but does not influence the upper canopy blade deflection driven by the canopy top shear. Thus, the extent of vortex penetration is considered the dominant factor controlling in-canopy flow and the associated mass transfer.

Physical modelling has provided a unique understanding of vegetation and flow interactions. In particular, rigid structures forming organised and irregular arrays have been widely used to study vegetation canopies, and have provided simplified, yet highly insightful, information to quantify fundamental flow characteristics (Ghisalberti & Nepf 2002; Liu *et al.* 2008; Chen, Jiang & Nepf 2013; Hamed *et al.* 2017; Chung *et al.* 2021). Vegetation increases drag, resulting in the formation of a shear layer at the canopy top and distinct turbulence (Gambi, Nowell & Jumars 1990; Nepf & Vivoni 2000). In flexible canopies, the vegetation deflection modulates the spatial and temporal dynamics, whereby canopy streamlining and drag reduction occur under sufficient hydrodynamic forcing (Ghisalberti & Nepf 2009; Luhar & Nepf 2011). Ikeda & Kanazawa (1996) observed intermittent, elliptical-shaped vortices forming at the canopy top that resulted in the so-called monami, evidenced by depression during the transit and waving motion of aquatic vegetation (see basic illustration in figure 1). Ghisalberti & Nepf (2002) defined this region as a mixing layer, whereby streamwise velocity fluctuations correspond to the Kelvin–Helmholtz (KH) frequency. As such, monami is driven by comparatively strong sweep events ($u' > 0$, $w' < 0$; where u' and w' denote the streamwise and vertical velocity fluctuations) at the vortex front, followed by a weak ejection ($u' < 0$, $w' > 0$) at the vortex rear, due to the downward and upward side of translational hairpin vortex evolution over the canopy (Ghisalberti & Nepf 2002, 2006; Finnigan, Shaw & Patton 2009; Okamoto & Nezu 2009). The influence of canopy motion and turbulence has also been
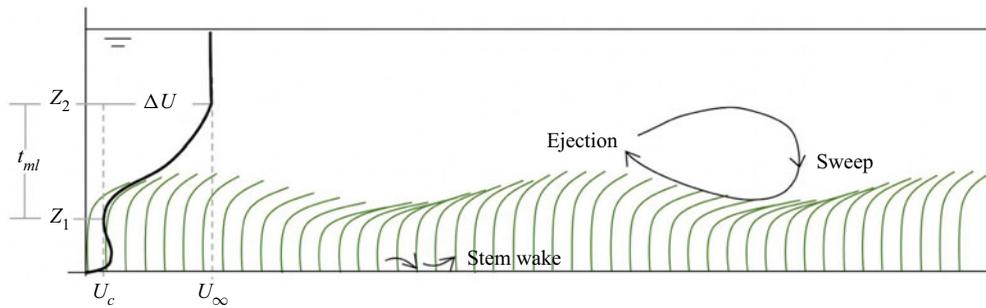
Figure 1. Basic features common in aquatic vegetation canopies. Here, t_{ml} represents the mixing layer and ΔU indicates the associated bulk velocity difference. Stem wake flow may not occur in fully flexible stems as discussed below.

investigated in wave- and wave–current-driven flows (Zeller *et al.* 2014; Zhang, Tang & Nepf 2018). However, the dynamics is not directly comparable, and the focus is placed on unidirectional flows herein.

Recent numerical modelling of flexible and semi-rigid canopies by Marjoribanks *et al.* (2017) revealed features of turbulent fluctuations corresponding to KH vortices within the mixing layer of the canopy, along with additional distinct turbulence scales associated with canopy motion. The unsteady blade dynamics of a flexible canopy remains partially understood, particularly with respect to the spatial quantification of turbulence and exchange within and above the canopy. The spatial dynamics of coherent vortices within the canopy mixing layer under a unidirectional flow has mostly been inferred using visualisation techniques with, for example, dye (Ghisalberti & Nepf 2005) and long exposure imaging (Christianen *et al.* 2013).

Comparatively few studies have conducted quantitative measurements of the spatio-temporal features of turbulence associated with aquatic vegetation canopies. Instantaneous flow measurements by Nezu & Sanjou (2008) using particle image velocimetry (PIV) showed the characteristics of coherent vortices for a flexible canopy, where coherent flow structures exhibited a greater degree of organisation near the vegetation edges than within the canopy. Okamoto & Nezu (2009) explored the interaction between flow and blade motion using a phase-averaged approach, revealing that maximum vertical momentum transport occurs when vegetation is at the maximum and minimum of the deflected heights. Sweep events appeared to penetrate the canopy, whereas ejections mostly remained above the canopy top. Okamoto, Nezu & Sanjou (2016) evaluated various canopy heights and noted that vortical structures are less coherent above a flexible canopy than over a rigid canopy, and do not penetrate into the lower parts of the canopy, the stem wake region. However, alteration to blade flexural rigidity associated with varying blade lengths was not accounted for, which has been found to influence canopy turbulence (Zhang *et al.* 2018). Cross-spectral analysis between flow velocity and blade deflection by Okamoto *et al.* (2016) showed that several rows could be deflected in phase with one another and in near unison, and the number of waving elements was dependent on the length scale of turbulence structures. Chen *et al.* (2013) also used PIV to evaluate time-averaged turbulence from the leading edge of a rigid canopy but did not acquire measurements for a flexible canopy, and optical constraints did not allow assessment of the flow structures within the canopy. A large fraction of the research regarding spatio-temporal processes has focused on the dynamics of the flow above canopies, especially in seagrass canopies. In contrast, understanding flow interactions within the

canopy are not well developed, despite their known importance to, for example, bed sediment transport processes. The research presented herein overcomes challenges of obtaining optical clearance within the canopy by employing refractive-index-matching (RIM) techniques using a dynamically equivalent flexible canopy.

Various studies have quantified coherent vortices and isolated blade motions, and distinct differences in motion and turbulence dynamics have been linked to canopy morphology. Singular flexible vegetation elements deflect to a greater extent than when located within a canopy (O'Connor & Revell 2019), thus altering the vertical distribution of stresses and canopy motion. Wilson *et al.* (2003) found that the presence of plant fronds, as opposed to a single rod, resulted in increased momentum absorption and turbulent mixing. Furthermore, vegetation foliage may promote a quasi-periodic velocity within the mixing layer due to the increased vortex coherence (Caroppi *et al.* 2019). O'Connor & Revell (2019) showed that monami behaviour is a function of the natural blade frequency and the mixing layer instability frequency, resulting in the spatial and temporal canopy dynamics being associated with combined fluid–structure interaction. The spatial configuration of the vegetation element within a canopy is also an important factor; Liu *et al.* (2008) noted a substantial reduction in streamwise in-canopy velocity when stems were staggered as compared with a linear arrangement. Importantly, these studies emphasise the importance of studying canopies that are comparable to natural environments. Geometrically and dynamically scaled models may enable representative canopy motion dynamics to be replicated and thus allow for the quantification of the hydrodynamics within aquatic canopies.

The dynamics of coherent flow structures and their spatio-temporal evolution above and within canopies remains poorly understood, particularly with respect to the interaction of coherent vortices associated with KH instability within canopies. This investigation focuses on the spatial and temporal dynamics of a canopy representative of the common seagrass species *Zostera marina*. The analysis is complemented by a comparative assessment of flows over and through a rigid canopy to provide a broader view of a diverse range of biota-flow environments, including coral reefs, salt marshes and mangroves. The use of a large-scale RIM methodology provides unobstructed optical access to flow structures throughout the canopies from bed to free stream, permitting the acquisition of high resolution spatial and temporal flow field measurements within a comprehensively scaled vegetation canopy. The set-up of the experimental facility and design of scaled vegetation is described in § 2. Statistics and spatio-temporal analysis of the turbulence are discussed in § 3, and the principal conclusions are given in § 4.

2. Experimental set-up

Turbulence within, and above, a surrogate aquatic seagrass and a rigid canopy was studied under various flow conditions (§ 2.2) in the large recirculating RIM flume at the University of Illinois. The facility has a test section of 2.50 m length, 0.45 m width and 0.5 m height, operated in free surface mode. The RIM was achieved by matching the refractive index of the polypropylene elements with the working fluid solution, thus rendering the vegetation nearly invisible when submerged and exposed to a 532 nm wavelength light. The working fluid consists of an aqueous sodium iodide (NaI) solution at approximately 63 % by weight, with density $\rho_f \approx 1780$ kg m^{-3} and kinematic viscosity $\nu \approx 1.1 \times 10^{-6}$ m^2 s^{-1}; its temperature is kept constant to ensure optimum optical access. Additional information on the RIM technique and facility are given in Blois *et al.* (2012, 2020) and Bai & Katz (2014).
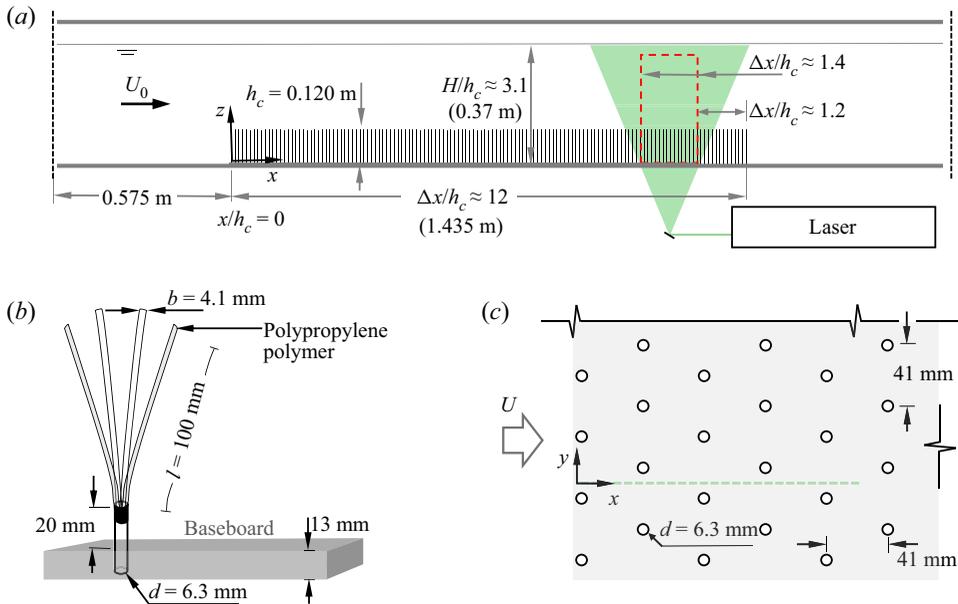
Figure 2. (*a*) Basic schematic illustrating surrogate, undeflected seagrass in the RIM test section, and the field of view; (*b*) details of a surrogate four-blade seagrass unit, and (*c*) top view of the staggered arrangement of the seagrass units; here, the dashed green line indicates the location of the PIV wall-normal plane.

2.1. *Surrogate seagrass canopy*

The flexible canopy design considered dynamic scaling representative of plant structures, as well as dimensions and mechanical properties of a common coastal seagrass species *Zostera marina* (de los Santos *et al.* 2016). Structural and morphological comparability also exists with freshwater eelgrass, specifically those under the genus *Vallisneria*.

Each flexible element of the canopy consisted of four rectangular blades, simulating vegetation leaves, attached to a rigid 20 mm long, cylindrical stem of diameter 6.35 mm; see figure 2. Dynamic scaling was achieved through assessment of two dimensionless parameters, namely, the Cauchy number, *Ca*, representing the ratio of drag to rigidity force, and the Buoyancy parameter, *B*, representing the ratio of buoyancy to rigidity forces (Luhar & Nepf 2016)

$$Ca = \frac{\rho_f b U_0^2 l^3}{EI} \quad \text{and} \quad B = \frac{(\rho_f - \rho_v) \, gbdl^3}{EI} \qquad (2.1a,b)$$

where ρ_v is the blade density, b and d are the blade width and thickness, l is blade length, U_0 is incoming bulk velocity defined by the cross-sectional area of the fluid and the incoming flow discharge, g is the acceleration due to gravity, E is Young's modulus and I ($=bd^3/12$) is the second moment of inertia.

Particular emphasis was placed on matching B due to the naturally large variability in *Ca* associated with the differing flow velocities considered herein. To achieve appropriate scaling, the blades were made from a polypropylene polymer of $\rho_v = 870 \pm 25$ kg m^{-3}, $b = 4.13 \pm 0.18$ mm, $d = 0.112 \pm 0.005$ mm, $l = 100$ mm and $E = 1.32 \pm 0.12$ GPa, resulting in $B = 6.59 \pm 0.80$. All error values indicate one standard deviation from the sample set mean ($n = 20$). The blades are comparable to the model *Zostera marina* blades implemented by Ghisalberti & Nepf (2002) and representation of *Posidonia australis* seagrass by Abdolahpour *et al.* (2018), with B values ranging from 6.43 to 7.06.

Scenario	Canopy	U_∞ (m s^{-1})	U_0 (m s^{-1})	Re (–)	Fr (–)	Ca (–)	Motion type	h_d (mm)	A_w (mm)
F1	Flexible	0.154	0.102	3.5×10^4	0.08	120	Swaying	93	5
F2	Flexible	0.220	0.156	5.3×10^4	0.12	279	Monami	74	–
F3	Flexible	0.284	0.206	7.0×10^4	0.15	489	Monami	65	9
F4	Flexible	0.351	0.260	8.8×10^4	0.19	777	Monami	55	–
F5	Flexible	0.413	0.312	1.1×10^5	0.22	1188	Monami	55	9
R1	Rigid	0.164	0.102	3.5×10^4	0.09	NA	NA	120	NA
R2	Rigid	0.242	0.153	5.2×10^4	0.13	NA	NA	120	NA
R3	Rigid	0.324	0.205	7.0×10^4	0.17	NA	NA	120	NA
R4	Rigid	0.403	0.256	8.7×10^4	0.21	NA	NA	120	NA
R5	Rigid	0.486	0.310	1.1×10^5	0.26	NA	NA	120	NA

Table 1. Summary of the experimental cases and basic parameters. U_∞ and U_0: free-stream and bulk velocities; Re, Fr and Ca: Reynolds, Froude and Cauchy numbers; h_d: mean canopy height, A_w: vertical amplitude of the canopy motions and NA: not applicable.

The resulting flexible canopy (henceforth referred to as surrogate seagrass or simply seagrass) had an undeflected height of $h_c = 120$ mm. Given that the blade geometry alters the reconfiguration behaviour (Albayrak *et al.* 2012), care was taken to ensure the consistent arrangement of blades around each stem (figure 2*b*). Vegetation elements were mounted in a staggered arrangement (figure 2*c*) at a density of 569 stems m^{-2} along a 1.435 m ($\Delta x/h_c \approx 12$) canopy length spanning the flume width. A roughly comparable rigid vegetation canopy was made with uniform acrylic rods of diameter $d_r = 6.35$, a height of $h_c = 120$ mm from the baseboard and vertically mounted in the same staggered configuration as the surrogate seagrass (figure 2*c*). This rigid canopy served as a complementary base case that helped to identify the role of motion associated with flexible canopies, along with providing an elementary analogue to mangrove pneumatophores and hard corals.

2.2. *Experimental conditions*

Two sets of five experiments were conducted for the surrogate seagrass and rigid canopy (table 1), where, $h_d = (h_{d,max} + h_{d,min})/2$ denotes the mean deflected canopy height, and $A_w = (h_{d,max} - h_{d,min})/2$ represents the vertical amplitude of the canopy oscillations in which $h_{d,max}$ and $h_{d,min}$ denote the average maximum and average minimum heights.

The surrogate seagrass and rigid canopy were investigated at Reynolds numbers, $Re = U_0 H_0/\nu \in [3.5 \times 10^4, 1.1 \times 10^5]$, ($Re_{R_h} = U_0 R_h/\nu \in [1.3 \times 10^4, 4.0 \times 10^4]$ based on the hydraulic radius, R_h), where U_0 is the incoming bulk velocity, and $H_0/h_c \approx 3.1$ ($H_0 = 0.373$ m) is the water depth at the flume entrance, and under subcritical conditions with Froude numbers of $Fr = U_0/\sqrt{gH_0} \leqslant 0.26$, where U_∞ is the free-stream velocity, and g is gravitational acceleration. Instantaneous flow fields were acquired at $x/h_c \geqslant 9.5$, with $x = 0$ denoting the beginning of the canopy. Bailey & Stoll (2016) noted that larger spanwise-oriented structures within a mixing layer maintain coherence. Image pairs were obtained using a high-speed, 4 MP (2560 pixels $\times$ 1600 pixels) CMOS camera with a 60 mm lens at a frequency of 100 Hz. The field of view (FOV) of the flexible canopy spanned $\Delta x/h_c = 2.2$ horizontally and extended $\Delta z/h_c = 1.6$ vertically from the bed. A complementary FOV covering $\Delta x/h_c = 1.4$ and $\Delta z/h_c = 2.2$ from the bed was also included, which provided a total of 2850 and 4940 image pairs for the rigid and flexible

cases, respectively. The FOVs were illuminated with a 1 mm thick light sheet provided by a 250 mJ pulse^{-1} double-pulsed laser supplied by TSI. The flow was seeded with 13 μm hollow glass silver-coated particles with a density of 1800 kg m^{-3}. Data processing of image pairs was conducted using TSI Insight 4G software with an interrogation window of 24 pixels × 24 pixels with 50 % overlap, providing a vector grid spacing of $\Delta x = 1.64$ mm and $\Delta z = 1.22$ mm.

2.3. *Basic features of the motions – visualisation*

The ten cases investigated covered various flow and blade motions with different degrees of interaction between flow above and within the canopy and seagrass oscillations. The blades underwent swaying for the lowest flow ($Re = 3.5 \times 10^4$, $Ca = 120$), and progressed into coherent waving motion representative of monami by $Re = 5.3 \times 10^4$, $Ca = 279$, which modulated the unsteady momentum exchange between the inner and outer canopy flows.

Supplementary movies available at https://doi.org/10.1017/jfm.2021.1142 illustrating the streamwise velocity fluctuations in the full FOV field within and above the seagrass (supplementary movie 1) and rigid canopy (supplementary movie 2) for the $Re = 1.1 \times 10^5$ (F5 and R5 scenarios; table 1) aid appreciation of the rich multiscale dynamics, and reveal the signature of coherent structures. Hereon, we analyse these flows and blade interactions and characterise the dominant motions and their role in seagrass dynamics and unsteady flow exchange.

3. Results

Here, we first quantify and discuss the flow statistics within and above the surrogate seagrass; then, we inspect spatial and temporal features of the dominant coherent motions. Comparison with a rigid canopy is also included to aid insight into specific processes induced by the surrogate seagrass.

3.1. *Temporally and spatially averaged turbulence statistics*

The canopy boundary layer and inner flow within the surrogate seagrass exhibited significant departure from the rigid counterparts, which were modulated largely by the blade swaying. Basic flow statistics within and above the flexible and rigid canopies for a representative case at $Re = 7.0 \times 10^4$ (i.e. F3 and R3 scenarios; table 1) evidence the impact of the surrogate seagrass on the flow. This is illustrated in figure 3 with the dimensionless streamwise velocity, U/U_∞, kinematic shear stress, $-\langle u'w' \rangle/U_\infty^2$, and turbulence intensity of the streamwise, σ_u/U_∞, and vertical, σ_w/U_∞ components. Here, $()'$ indicates temporal fluctuations and σ and $\langle \rangle$ denote the standard deviation and time-averaging operators.

The deflected blades significantly restricted the mass flux within the surrogate seagrass and enhanced the turbulence surrounding the top as compared with the rigid canopy. This resulted in a sharper mean shear that promoted unsteady exchange with the external flow, resulting in increased kinematic shear stress and turbulence levels. This, in turn, promoted oscillations of the canopy elements, which enhanced unsteady flow exchange and flow fluctuations near the top of the surrogate seagrass. The degree of such two-way interaction between the flow and blade motions is embodied in the Cauchy number. Evaluation of scenarios encompassing a range of *Ca* provides context for natural flows, and offers a way
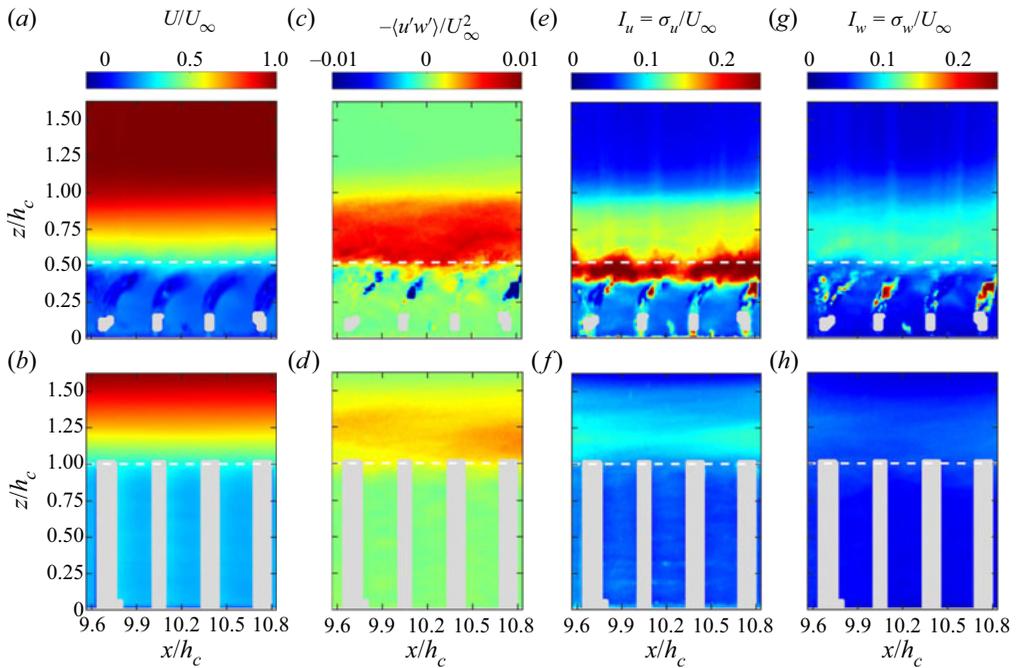
Figure 3. Time-averaged streamwise velocity U/U_∞, kinematic shear stress, $-\langle u'w'\rangle/U_\infty^2$, and turbulence intensity of the streamwise, $I_u = \sigma_u/U_\infty$, and vertical, $I_w = \sigma_w/U_\infty$, velocity components within and above the surrogate seagrass (a,c,e,g) and rigid canopy (b,d,f,h) at $Re = 7.0 \times 10^4$ (F3 and R3 scenarios; table 1). The horizontal, white dashed lines approximately mark the inner (within canopy) and outer flows.

to uncover several processes, including the control of flow fluctuations and particulate transport.

Double averaging in the streamwise direction and time (figure 4) illustrates distinct features of the bulk flow statistics across the vertical span for a range of *Re* in the seagrass and rigid canopy. The vertical axis is split into two non-dimensional regions to aid understanding of the effect of the deflection of the flexible canopy. The canopy region is normalised by the mean deflected canopy height, i.e. z/h_d; whereas the region above the canopy is normalised as $z_A = (z - h_d)/h_c + 1$. This factor sets the relative canopy top as a secondary origin. Note that the non-dimensional streamwise velocity, U/U_∞ profiles collapse very well within and above the rigid canopy and z_A is not normalised by the boundary layer depth, δ, to stress the flow variability induced by the flexible canopy. In contrast to the seagrass, the rigid canopy did not alter development of the boundary layer at the *Re* analysed. It is also worth highlighting the changing profiles within the seagrass canopy with changes in *Re*. This is further illustrated by the velocity change $\Delta U/U_\infty = (1 - U_c/U_\infty)$ within and above the canopies (figure 5a), which is approximately constant for the rigid canopy but decreases with *Re* in the seagrass experiments.

A distinct effect induced by the surrogate seagrass is the relative height of the maximum kinematic shear stress (figure 4b), which does not occur within the vicinity of the mean canopy top due to the particular modulation of the blade oscillations. Note the lower kinematic shear stress compared with, e.g. Ghisalberti & Nepf (2006) and Chung *et al.* (2021). This is due to the shorter canopy length L_c and the relative FOV location. Indeed, the canopy length $L_c = 1.435$ m (figure 2a) is shorter than those in Ghisalberti & Nepf (2006) and cases in Chen *et al.* (2013) and Chung *et al.* (2021). As pointed out by
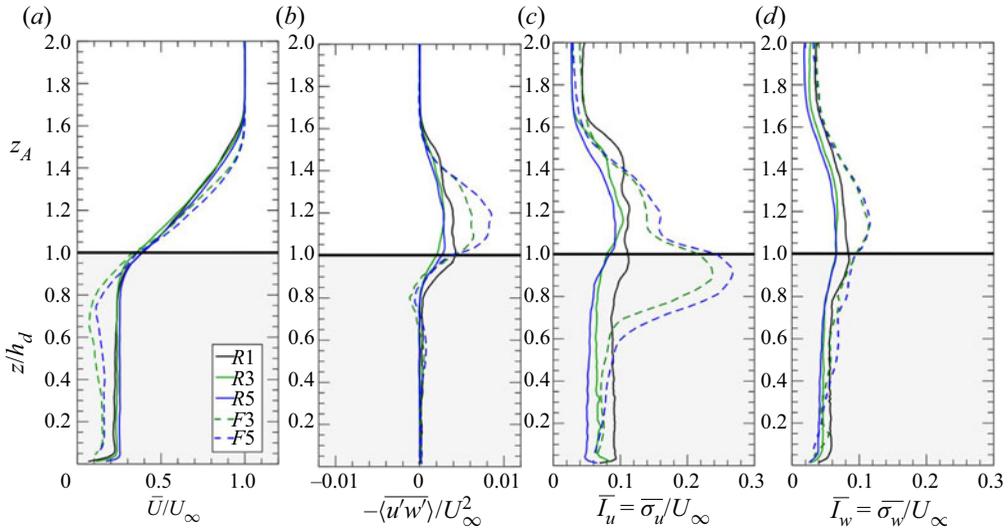
Figure 4. Space- and time-averaged vertical profiles of the normalised (*a*) streamwise velocity $\bar{U}/U_\infty$, and (*b*) kinematic shear stress $-\langle \overline{u'w'} \rangle/U_\infty^2$. Turbulence intensity of the streamwise (*c*) $\bar{I}_u = \overline{\sigma_u}/U_\infty$ and vertical (*d*) $\bar{I}_w = \overline{\sigma_w}/U_\infty$ velocity components. The overbar denotes space-averaging. Vertical axis is normalised by the deflected canopy height h_d, and the shaded area represents the data within the canopy.
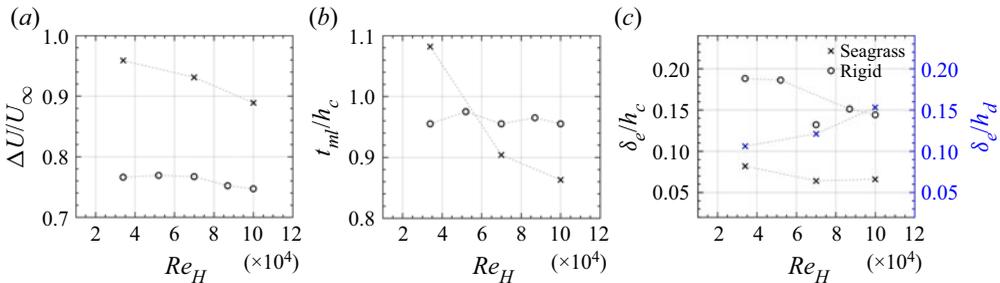
Figure 5. (*a*) Velocity change within canopy, (*b*) mixing layer thickness, (*c*) vortex penetration depth relative to the undeflected canopy height (left axis) and vortex penetration relative to the deflected canopy height (right axis). Data are shown for both the flexible seagrass and rigid canopy.

Chung *et al.* (2021), the maximum shear stress increases with L_c. Additionally, our FOV measured the developing region of the mixing layer. Chen *et al.* (2013) showed that the development length $X_* \approx (8 \pm 2)U_v L_S/u_*|_{h_c}$, where U_v, L_S and u_* are the vortex convection velocity, shear length scale and friction velocity at the canopy top; Chung *et al.* (2021) showed that the shear length scale can be estimated as $L_s = \bar{U}/\partial \bar{U}/\partial z|_{h_c}$, resulting in $L_s \approx 0.04$ m and $X_* \approx 1.75 \pm 0.44$ m for the R1 case. This indicates that our FOV is in the developing region of $\approx 0.72 X_*$, which also leads to lower kinematic shear stress, as shown in Chen *et al.* (2013) and Chung *et al.* (2021). It is worth stressing the importance of this region given the heterogeneity or patchiness of natural canopies affected by various topographic factors and morphological features, including width, shape factor, rigidity and orientation of the blades. Remarkably, the associated streamwise component, expressed here as turbulence intensity $\bar{I}_u$, occurred below the mean canopy height. The particular locations of the maximum in $-\langle u'w' \rangle$ at $z/h_d > 1$ and $\langle u'u' \rangle$ at $z/h_d < 1$ in the seagrass indicate a transport modulated by the motion of the blades, which is very different from

the rigid counterpart and represent a signature of the distinct scale-to-scale dynamics. The higher turbulence momentum flux above the seagrass canopy, indicated by larger magnitude $-\langle u'w' \rangle$, suggests greater mass transfer within the canopy. The deflection of flexible blades during the passage of coherent vortices reduces the exposed blade surface area, and thus the potential uptake of e.g. dissolved inorganic nitrogen relative to separated blades during weaker flows (Weitzman *et al.* 2013). Furthermore, the extent of the $-\langle u'w' \rangle$ within the canopies (figure 4*b*) provides an indication of the vortex penetration depth, δ_e, given by the distance below h_d whereby kinematic stress decreases to 10 % of the maximum (Nepf & Vivoni 2000). Evaluation of vortex penetration depth normalised by deflected canopy height (h_d) indicates vortex penetration towards the bed was smaller for the flexible canopy than the rigid canopy at lower *Re*, but increased with larger *Re* (figure 5*c*).

The mixing layer thickness, $t_{ml} = z_2 - z_1$, where z_1 and z_2 denotes the height of the 99 % free-stream and in-canopy velocities, remained nearly constant for the rigid canopy with *Re* (figure 5*b*), with an asymmetrical vertical distribution with approximately one third below h_c, similar to the observations of Ghisalberti & Nepf (2004). Ghisalberti & Nepf (2002) found monami occurred when $t_{ml}/h_d > 1.5$–2.1, which is the case here, whereby t_{ml}/h_d ranges between 1.4 and 2.0, with the lowest *Re* condition not initiating coherent waving representative of monami. Ghisalberti & Nepf (2002) also noted that waving increases the vortex penetration depth (normalised by h_d) and suggested that waving canopies induce a weaker momentum sink compared with rigid cases. However, Nepf & Ghisalberti (2008) reported no difference in dimensional δ_e vs waving and un-waving canopies. Alternatively, when evaluated in dimensional terms based on the fixed dimension of h_c, the flexible canopy vortex penetration depth does not increase with *Re* and remains smaller than the rigid canopy, revealing that the flexible canopy limits the depth of stresses (see figure 5*c*). It is worth pointing out that Okamoto & Nezu (2009) inspected penetration of coherent structures within a flexible canopy composed of an array of single elements and suggested that, regardless of differences in vegetation morphology, the role of canopy reconfiguration associated with flexibility plays a dominant role in reducing the vertical penetration of stresses. However, Wilson *et al.* (2003) noted the role of foliage morphology, where a smaller penetration of turbulent stresses occurred for rods with fronds (similar to flexible blades) than rods alone, and suggested that the presence of the fronds limited the momentum exchange between the canopy and overlying flow.

The redistribution of the Reynolds stresses induced by the seagrass can be further assessed by inspecting the velocity fluctuations into four quadrants, namely Q_1: $u' > 0$, $w' > 0$ (outward interactions), Q_2: $u' < 0$, $w' > 0$ (ejections), Q_3: $u' < 0$, $w' < 0$ (inwards interactions) and Q_4: $u' > 0$, $w' < 0$ (sweeps). Specifically, figure 6 illustrates the spatial distribution of the sweep-to-ejection ratio, Q_4/Q_2, for selected cases. Consistent with Yue *et al.* (2007), Poggi *et al.* (2004) and Chen *et al.* (2013), the base cases with the rigid canopy exhibited a predominance of sweeps within the canopy for all *Re* tested. However, ejections dominated within the surrogate seagrass with comparatively strong sweeps in the vicinity of the mean canopy height. Note also the distinct modulation of the blade motions in the distribution of $Q4/Q2$ in the boundary layer. Although sweep-dominated events appear on the rigid canopy at the *Re* studied, those were only present in the lower half of the flexible canopy ($z/h_d < 0.5$) at the lowest *Re* (figure 6*a*); the minimal blade deformation at that *Re* made it comparable to that in the rigid canopy. Figure 6 also shows a phenomenon not previously reported, namely, the transition to ejection-dominated events with *Re* within the seagrass. The upward motion of the blades associated with the ejection at the rear of vortices may result in ejection events. Likewise, the deflection of blades prevents penetration of sweep events as per the rigid canopy. This is also consistent with
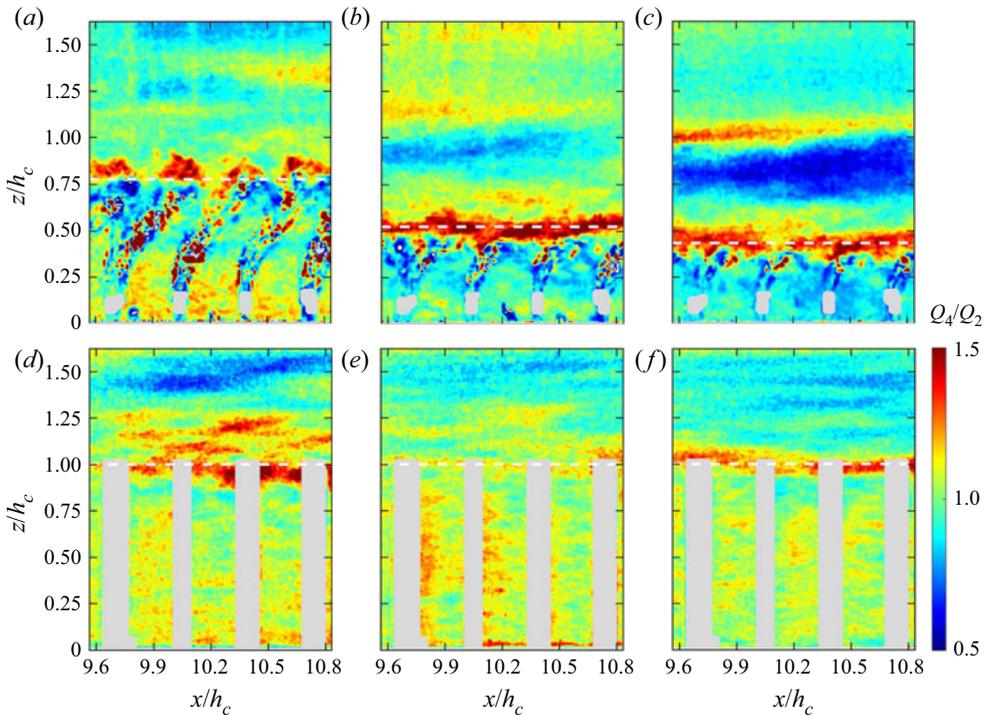
Figure 6. Ratio of total contribution of sweep ($Q4$) and ejection ($Q2$) events for the seagrass scenarios (*a*) F1, (*b*) F3, (*c*) F5 and rigid canopy cases (*d*) R1, (*e*) R3, (*f*) R5. Dashed white lines indicate the mean canopy height.

the arguments by Okamoto *et al.* (2016), who pointed out that coherent structures do not extend into the lower canopy region under monami.

The region with the largest sweep-dominated motions was consistently located at the vicinity of the mean deformed seagrass height, h_d, in agreement with other findings (Nezu & Sanjou 2008; Marjoribanks *et al.* 2017). The differences in the magnitude of the sweep-to-ejection ratio between the surrogate seagrass and rigid canopy are likely due to the ability of the blade motion to promote turbulent transport. Bailey & Stoll (2016) suggested that a canopy impedes a vortex to draw fluid from below, thus limiting the presence of ejections near the canopy top. In contrast, sweeps dominate due to their ability to draw flow fluctuations from the unobstructed and higher momentum flow above. The deflection of blades also increases the canopy top blockage area, producing an apparent increase of the canopy density, which likely increases sweep dominance (Poggi *et al.* 2004). In contrast, the upright blades of the rigid canopy do not provide the same top-down area blockage and constraint. Importantly, this suggests that the streamlining of the flexible canopy blades under sufficient flow results in an effective barrier to larger-scale turbulence.

3.2. *On the coherent motions and flow–canopy interaction*

First, we explore the combined redistribution, enhancement and damping of turbulence across relevant scales modulated by the blade motions within and above the canopy with the one-dimensional compensated spectra of the streamwise velocity fluctuations, $f\phi(f)$, where f is the frequency. Figure 7 shows this quantity normalised by the maximum value, $f\phi^* = f\phi/\max\{f\phi\}$, throughout the vertical span at nearly the centre of the
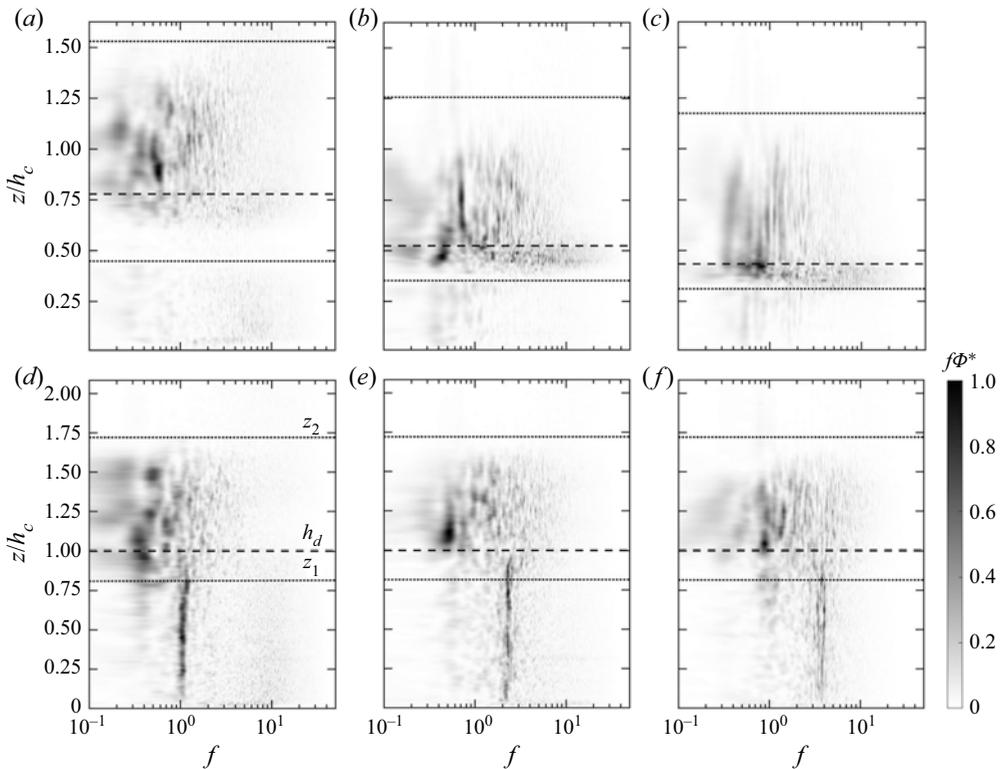
Figure 7. Compensated one-dimensional spectra of the streamwise velocity fluctuations along the vertical span at the centre of the FOV $x/h_c = 10.25$ for (*a*) F1, (*b*) F3 and (*c*) F5 seagrass scenarios, and (*d*) R1, (*e*) R3 and (*f*) R5 rigid canopy cases. Dashed lines indicate the canopy top (h_d), and dotted lines denote the location of z_1 and z_2.

FOV ($x/h_c = 10.25$). A low-pass filter with a 10 Hz cutoff frequency is applied to the signal; over that frequency, the energy contribution is minor. The spectral velocity distributions within the rigid canopy at three Re show a comparatively dominant energy at a frequency $f_0 = f_0(Re)$, corresponding to vortex shedding from the rigid structures, where the Strouhal number is $St = f_0 d_r/U_1 \approx 0.19$–$0.20$ (Norberg 1994). Such motions are missing within the seagrass; there, the turbulent energy plays a minor role compared with the above-canopy turbulence and that within the rigid canopy.

Generation of KH instability (Ghisalberti & Nepf 2002; Okamoto & Nezu 2009; Okamoto *et al.* 2016; Marjoribanks *et al.* 2017) appears to be associated with enhanced energy above the canopy. Considering Ghisalberti & Nepf (2002), the KH frequency, f_{KH}, can be estimated as follows:

$$f_{KH} = St\frac{\bar{U}}{\theta}, \quad \theta = \int_{-\infty}^{\infty} \left[\frac{1}{4} - \left(\frac{U - \bar{U}}{\Delta U}\right)^2\right] dz, \quad (3.1a,b)$$

where $\bar{U} = (U_\infty + U_c)/2$ (see figure 1), θ is the momentum thickness and $\Delta U = U_\infty - U_c$ is the bulk shear magnitude. In scenarios of unforced mixing layers $St \approx 0.032$, and varies modestly with the velocity ratio $R = \Delta U/(2\bar{U})$ by up to 5 % between $R = 0$ and 1 (Ho & Huerre 1984). The canopies, however, induce a distinct forcing such that the $St = 0.032$ for parallel, unforced flows is not quite applicable. Indeed, Mandel *et al.* (2019)

934 A17-12

Scenario (–)	St (–)	R (–)	f_n (Hz)	f_{max} (Hz)	f_{KH} (Hz)
F1	—	0.92	0.34	0.21	0.17
F3	—	0.87	0.34	0.13	0.36
F5	—	0.80	0.34	0.37	0.54
R1	0.20	0.62	NA	0.15	0.24
R3	0.19	0.62	NA	0.52	0.50
R5	0.20	0.60	NA	0.88	0.74

Table 2. Characteristic parameters in the surrogate seagrass and rigid canopy. Strouhal number St, velocity ratio R, estimated blade natural resonance frequency f_n, predicted KH frequency f_{KH} and time-averaged peak spectral frequency at $z/h_d = 1.05$, f_{max}. NA: not applicable.
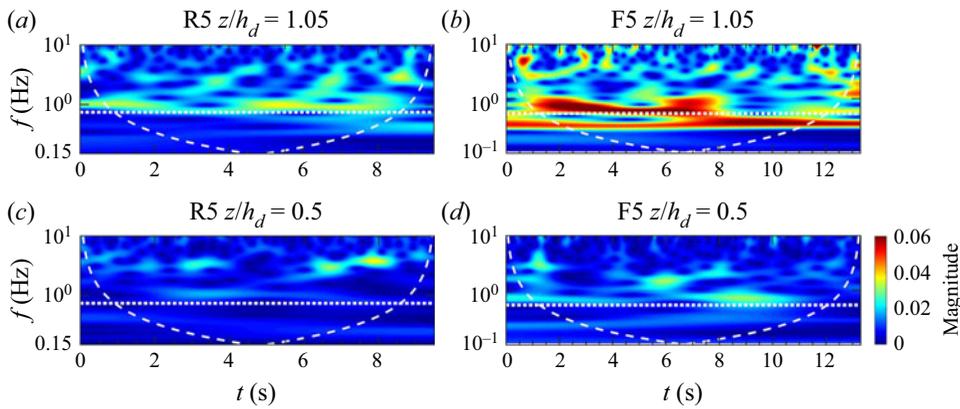
Figure 8. Wavelet representation of the streamwise velocity within and immediately above the flexible (F5) and rigid (R5) canopies at $Re = 1.1 \times 10^5$. (*a*) R5, $z/h_d = 1.05$, (*b*) F5, $z/h_d = 1.05$, (*c*) R5, $z/h_d = 0.5$, (*d*) F5, $z/h_d = 0.5$. White dashed lines indicate the cone of influence, and horizontal dotted lines mark f_{KH}.

obtained $St = 0.064$ for a rigid canopy. This illustrates the possible differences between predicted and measured frequencies presented in table 2. Another characteristic frequency of interest is the undampened natural blade frequency, estimated by

$$f_n \approx C_n \sqrt{EI/l^4 \left(\rho_v bd + \rho_f C_M (\pi b^2/4) \right)}, \tag{3.2}$$

with $C_n = 0.56$ and $C_M \approx 1$ (Luhar & Nepf 2016), which results in $f_n \approx 0.34$ Hz. Recent numerical simulations by O'Connor & Revell (2019) indicate that canopy motion is a coupled response between the natural structure (vegetation blade) and coherent flow motions. Both f_n and f_{KH} may coexist if they differ sufficiently; however, a lock-in phenomenon and canopy waving may occur when f_n and f_{KH} are similar. The transition of two modes to lock-in behaviour is captured in figure 8(*b*), where a weaker shear is seen to lead to a smaller f_{KH} at $t \geqslant 8$ s, resulting in synchronisation.

A complementary inspection into the time–frequency domain with a Morlet wavelet analysis, reveals insightful features of the turbulent fluctuations in the canopy mixing layer and compact signatures within the period of the measurements, which can be obscured with velocity spectrum analysis. The cases for the highest Re (seagrass, F5, and rigid canopy, R5) scenarios are shown in figure 8 within the canopy at $z/h_d = 0.5$

and immediately above the mean canopy height at $z/h_d = 1.05$. The frequency associated with the predicted KH instability, f_{KH}, is indicated with horizontal dashed lines.

Note that the rigid canopy exhibits relatively energetic fluctuations at a frequency $f \geqslant f_{KH}$ with higher persistence at $z/h_d = 1.05$ (figure 8a). Remarkably, the velocity fluctuations in the surrogate seagrass exhibit two dominant, stronger signatures than those of the rigid canopy. One is a non-persistent, shear-induced f_{KH}, whereas the other is a persistent, blade-modulated signal at a lower frequency. These two distinct motions induced secondary motions between these frequencies for a short time (see figure 8b). Such an aperiodic phenomenon evidences additional nonlinearities induced by the large deformations of the blades (Jin *et al.* 2018).

Spatio-temporal characteristics of the flow fluctuations within the canopies at $z/h_d = 0.5$ reveal distinct energetic processes contributing to the dynamics. Numerical simulations by Marjoribanks *et al.* (2017) noted that f_{KH} was not persistent within the mixing layer in semi-rigid and flexible canopies. Here, in the rigid canopy, the flow exhibits dominance of the cylinder shedding frequency; it is not continuous across the timespan (see figure 8c). In contrast, flow in the seagrass shows the signature of KH motions at times during coordinated blade motions (see supplementary movie 1), which promoted the generation of KH-like motions into the canopy (see figure 8d). Under uncoordinated blade motions, there is a lack of KH-like motions. The averaged vortex penetration remains reduced by the seagrass under uncoordinated blade motions.

Inspection of selected instants offers insight into the underlying effects of the sweeps and ejections. In particular, the seagrass F5 case is considered herein, using two points for interrogation, with one above and one within the canopy at nearly the centre of the FOV, $(x/h_c, z/h_d) = (10.25, 1.3)$ and $(10.25, 0.4)$. From the resultant time series of u'/U_∞, w'/U_∞, and associated $-\langle u'w' \rangle/U_\infty$, we can observe instants with sweeps (e.g. $t = 4.25$ s, 5.91 and 7.30 s) and ejections (e.g. $t = 5.28$ s and 6.46 s). The time series and selected times are indicated in figure 9(a). The red lines correspond to instants with alternating u' above and within the canopy. Above the canopy, the sweep events correspond to positive u' and negative w', while ejection events express the opposite trends. The $u'w'$ values peaked with each event, yet the weak ejection event at $t = 5.28$ s represents a notably lower Reynolds shear stress. The behaviour within the canopy is less clear, which may suggest a lag in processes between the two regions.

The associated whole flow fields at the instants selected are shown in figure 9(b). The canopy experienced a depression of the blades in correspondence with the sweep events, followed by upward motion during ejection events. This waving motion of the canopy is comparable to previously reported monami processes (Ikeda & Kanazawa 1996; Ghisalberti & Nepf 2002). Details of the motions are shown in the supplementary movie 1.

Specific, quantitative insight into the key coherent structures and their dynamics can be obtained with SPOD. As a data-driven modal analysis technique, SPOD utilises empirical data and combines the merits of the traditional space-only POD and dynamic mode decomposition (DMD). SPOD extracts structures that are spatially and temporally coherent instead of the spatial-only coherence of POD. The SPOD modes are also optimal-averaged DMD modes (Tu *et al.* 2014), which contain the inherent energy ranking and form on an orthogonal basis for the flow field, like the POD-based techniques first proposed by Lumley (1970). Herein, the SPOD approach follows Sieber, Paschereit & Oberleithner (2016).

First, the so-called Welch method is used to construct an ensemble of realisations of the temporal Fourier transform of the data from a single time series consisting of N_T snapshots by breaking it into several segments. Each of these consists of N_{FFT} snapshots, and
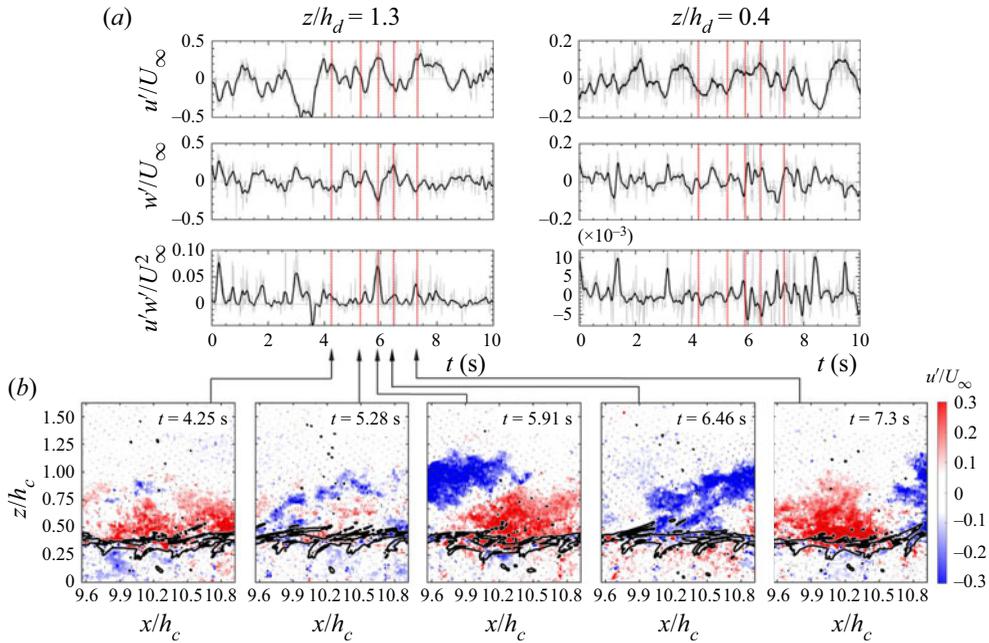
Figure 9. (*a*) Selected snapshots of the streamwise velocity fluctuations for the F5 case; sweeps at $th_d/U_\infty = 0$, ≈ 0.2 and ≈ 0.4 and ejections at intermediate times $th_d/U_\infty \approx 0.1$, and ≈ 0.3. The blades around the top are shown with black lines. (*b*) Time series of streamwise, u'/U_∞, and vertical, w'/U_∞, velocity fluctuations and kinematic shear stress, $-\langle u'w' \rangle /U_\infty$, at $z/h_d = 1.3$ and $z/h_d = 0.4$ at $x/h_c = 10.25$. The vertical red lines correspond to the instants in (*a*).

overlaps with the next segment are preferred to account for the statistical variability of the turbulent flow. Here, $N_T = 9000$, is the number of the zero-padding snapshot series, and $N_{FFT} = 1024$, which allowed us to achieve a resolution in the frequency domain of ≈ 1 Hz. A discrete Fourier transform is then applied on the separated time-dependent segment realisations, $q_{T_j}^k$, where k stands for the kth realisation of the vector of observations, and T_j is the instant. It allows us to obtain the coefficient $\hat{q}_{f_m}^k$ in the Fourier domain, where

$$\hat{q}_{f_m}^{(k)} = \sum_{j=0}^{N_{FF}-1} q^{(k)} \left(t_{j+1} \right) \exp(-\mathrm{i}2\pi jm/N_{FFT}), \quad k = -N_{FFT}/2 + 1, \ldots, N_{FFT}/2.$$

$$(3.3a,b)$$

Then, for each frequency f_m, $\hat{Q}_{f_m}$ may be formed as follows:

$$\hat{Q}_{f_m} = \begin{bmatrix} | & | & & | \\ \hat{q}_{f_m}^{(1)} & \hat{q}_{f_m}^{(2)} & \cdots & \hat{q}_{f_m}^{(N)} \\ | & | & & | \end{bmatrix}, \quad \hat{Q} \in \mathbb{C}^{M \times N} \qquad (3.4)$$

where M is the degree of freedom given by the number of spatial points in the x- and z-directions in each case, and N is the number of realisations. Singular value decomposition is then performed in each $\hat{Q}$ matrix.

We use the variance norm of a two-dimensional, two-component stochastic velocity fluctuations matrix $\underline{u}'(x, z, t) = [u'w']^T$ for the SPOD input. Modes are optimised in the mean square value of the velocity fluctuations by utilising singular value decomposition
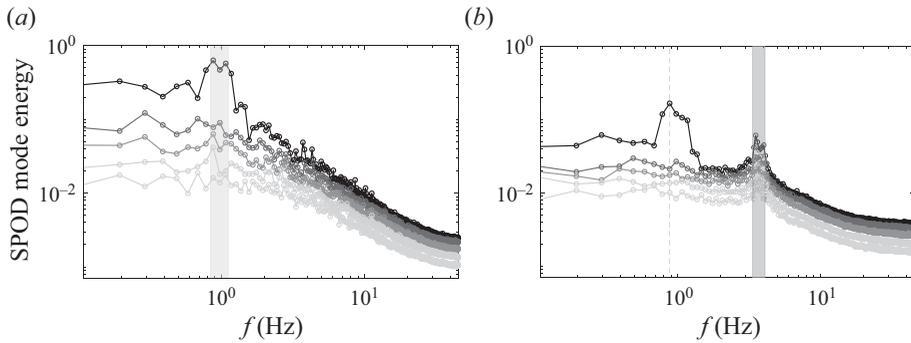
Figure 10. Spectral proper orthogonal decomposition (SPOD) spectra of the rigid R5 case of the flow field (*a*) above and (*b*) within the canopy, with the darkest (black) line being the first SPOD mode and the lighter lines the subsequent SPOD modes.

(Taira *et al.* 2017). Further details regarding SPOD implementation are given in Schmidt & Colonius (2020) and SPOD applications in Towne, Schmidt & Colonius (2018) and Schmidt *et al.* (2018).

Application of the SPOD, particularly for the rigid R5 and seagrass F5 cases, reveals particular features of the coordinated dynamics of the flow and seagrass, and the role of energetic coherent motions. Figure 10 shows the SPOD spectra above and within the canopy of the rigid case R5, and demonstrates the mode ranking characteristic of the SPOD method. The separation between the first and lower energy modes is prominent at a lower frequency ($\lesssim 3$ Hz) and suggests that the dynamics of large coherent structures can be approximated by the first few modes using a lower rank approximation. A broader band frequency of the dominant KH-type instability occurs above and within the rigid canopy. In contrast, a higher frequency peak is observed within the canopy (figure 10*b*) in agreement with the two-dimensional spectra in figure 7. The spatial mode shapes associated with the dominant frequencies of the streamwise SPOD modes, $\phi_{u'}$, are illustrated in figure 11, with the red–blue colour representing the spatially correlated patterns. The mode shapes above the canopy tip demonstrate structural features consistent with the shear layer KH instability (table 2); local changes of the convective velocity cause the observed broad frequency distribution. The von Kármán vortex street past the rods exhibited the well-known Strouhal relationship, $St \approx 0.2$.

Insight from the SPOD spectra above and below the seagrass at the same *Re* for the F5 case, can be obtained from figure 12. Coherent motions related to the KH frequency dominate above and below the canopy, and the corresponding mode shapes are shown in figure 13. While KH vortices have previously been discussed above seagrass canopies (Ghisalberti & Nepf 2002), and coherent vortices have been observed (Nezu & Sanjou 2008), these results provide compelling evidence of KH-type vortices and provide spatio-temporal information. A weaker local peak at 2.25 Hz present above the canopy suggests the existence of a weaker coherent structure (figure 13*a*2). However, this coherent structure with lower energy content is not able to penetrate the barrier created by the blade motion and thus is not observed for the in-canopy flow. Also, a mismatch exists between the primary mode frequency of the flow above and within the canopy, with the upper flow having the strongest mode at ≈ 0.4 Hz and the lower part at ≈ 0.6 Hz.

To uncover particular effects of the blade motion on flow interaction above and within the canopy, SPOD is performed on the full F5 case (figure 14). Close inspection shows that the most energetic modes at ≈ 0.4 Hz captured only the coherent structures above
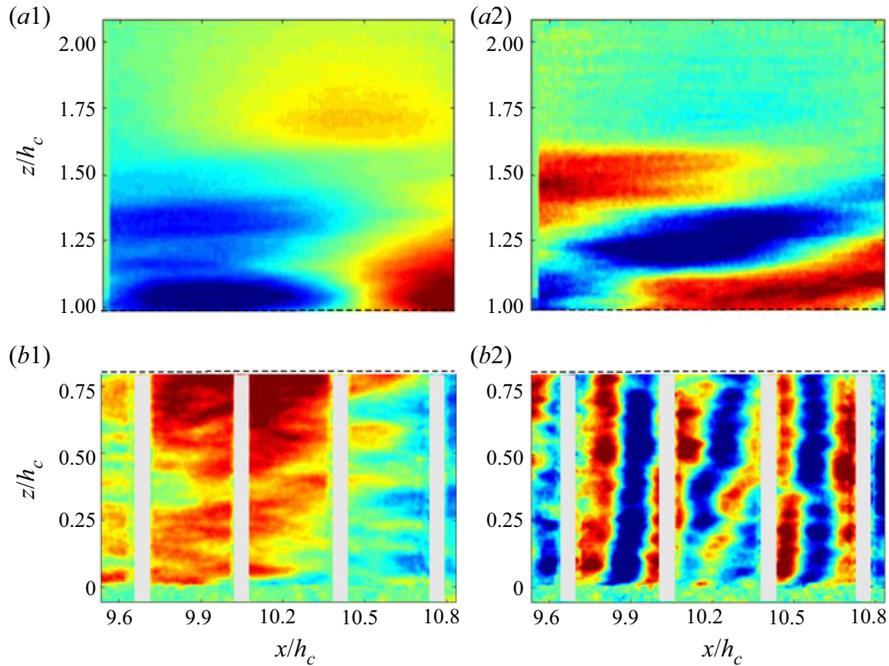
Figure 11. Spatial organisation of the first SPOD modes above the rigid R5 canopy at $f = (a1)$ 0.88 Hz and $(a2)$ 1.07 Hz; and within the canopy at $f = (b1)$ 0.88 Hz and $(b2)$ 3.52 Hz.
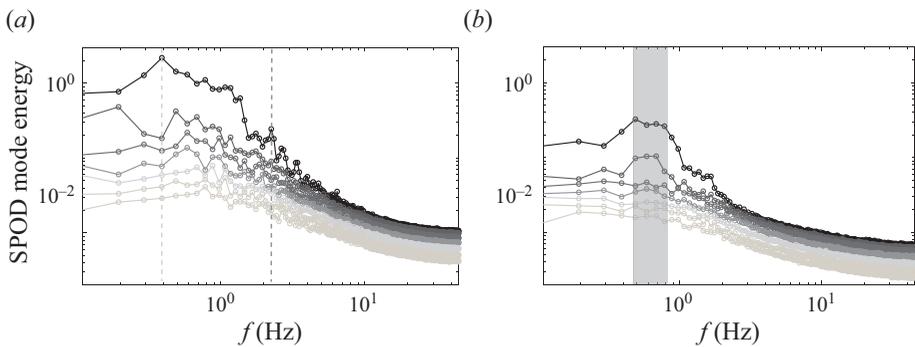

Figure 12. SPOD spectra of the seagrass, F5 case, of the flow field (a) above and (b) within the canopy, with the darkest (black) line being the first SPOD mode and the lighter lines the subsequent SPOD modes.

the canopy, whereas monami effects and entrainment of the coherent structures are better captured by the second strongest mode (see also supplementary movie 3). The inset shows the projected second mode time coefficient for the natural blade frequency and the KH frequency. Figure 15 illustrates a sequence every $\Delta th_d/U_\infty \approx 0.05$ within one period of the 0.6 Hz projected time coefficient. It reveals the streamwise propagation features and a monami effect with entrainment into the region within the canopy, which is not observed at 0.4 Hz due to a much weaker second mode despite its stronger first mode energy. The lack of sinusoidal-like behaviour exhibited in the 0.4 Hz projected-coefficient second mode, as compared with the 0.6 Hz counterpart, indicates that blade motion is dominated by the KH frequency rather than the natural frequency, consistent with figure 9.
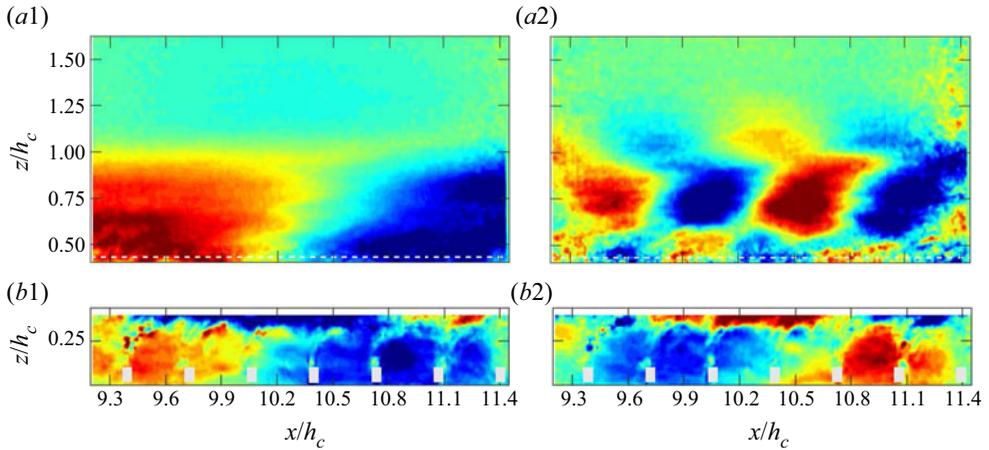
(a1) (a2)

Figure 13. Spatial organisation of the first SPOD modes above the canopy at $f = $ (a1) 0.4 Hz and (a2) 2.25 Hz; and within the canopy at $f = $ (b1) 0.6 Hz and (b2) 0.68 Hz.
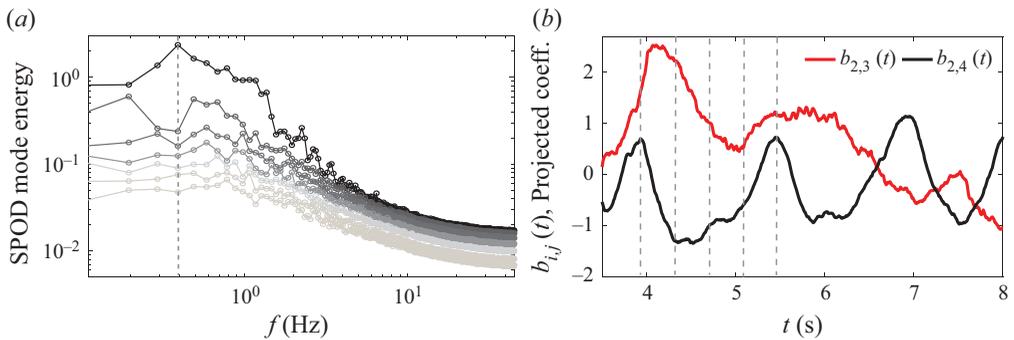
(a) (b)

Figure 14. (a) Full flow field SPOD spectrum on the seagrass F5 case. The darkest to lighter lines indicate the progression from the first to the fourth SPOD modes; (b) projected SPOD mode coefficients, $b_{i,j}(t)$ for the ith mode of j frequency.
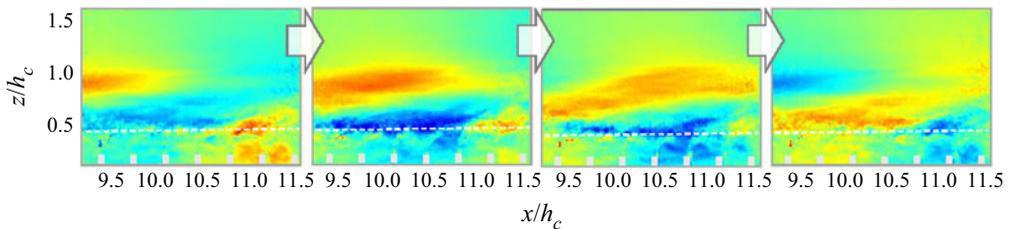

Figure 15. Sequence uniformly distributed in a period of the second SPOD mode of $f = 0.6$ Hz for the F5 seagrass scenario.

This description motivates inspection of the instantaneous quadrant analysis data given in figure 16(a). The 0.6 Hz peak supports our previous assumption that the switch from sweep-dominated to ejection-dominated behaviour within the flexible canopy is related to monami and the blade motion. The projected-coefficient first mode at 0.6 Hz is shown in figure 16(b). Combining this with the base analysis of §3.1 and figure 9,
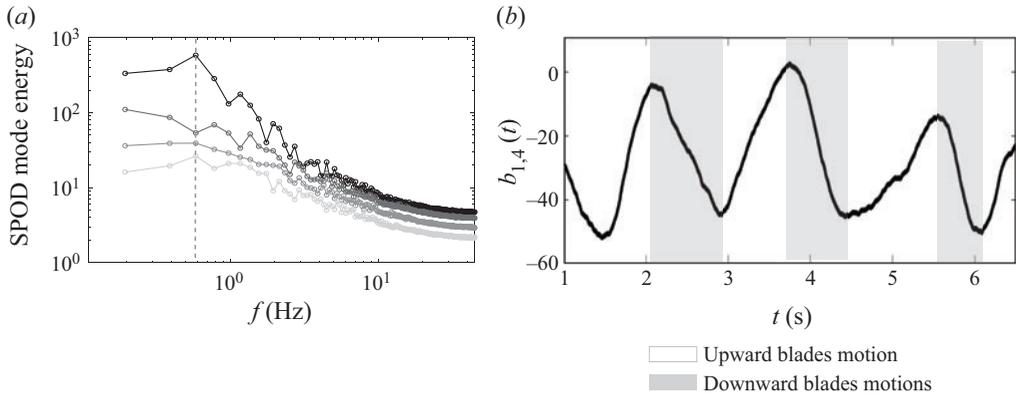
934 A17-18

Figure 16. (*a*) SPOD spectra form the quadrant analysis of the seagrass F5 case. The darkest to lighter lines indicate the progression from the first to the fourth SPOD modes; (*b*) projected SPOD mode coefficients, $b_{1,4}(t)$ for the first mode of 0.6 Hz.
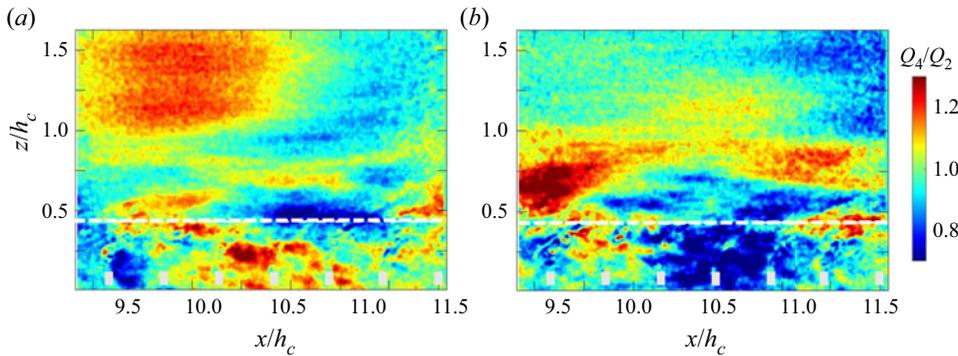

Figure 17. Conditional average of sweep to ejection ratio during the F5 flexible canopy (*a*) downward motion phase and (*b*) upward motion phase.

it is inferred that the projected-coefficient period is associated with the canopy blade motion. The conditional sampling method provides a representation of the sweep- or ejection-dominated flow within the canopy during the phase of downward and upward blade motions (figure 17). This supports our conjecture, whereby the presence of strong ejections within the flexible canopies correspond to the upward blade motions, which coincides with the rear of the KH vortex, and previously identified above-canopy ejection events shown in figure 9 and in past research (Ghisalberti & Nepf 2002; Okamoto & Nezu 2009). These results reveal the complexity and diversity of within canopy processes, which are driven by the canopy motion.

4. Conclusions

As highlighted in § 1, this investigation aims to contribute to our limited understanding of the dynamics of the dominant coherent flow structures and their spatio-temporal evolution above and within a canopy representative of common seagrass species. Our set-up enabled close inspection, identification and evaluation of energetic vortices and their space–time variability. The large body of previous research on canopy flows aligns with our initial
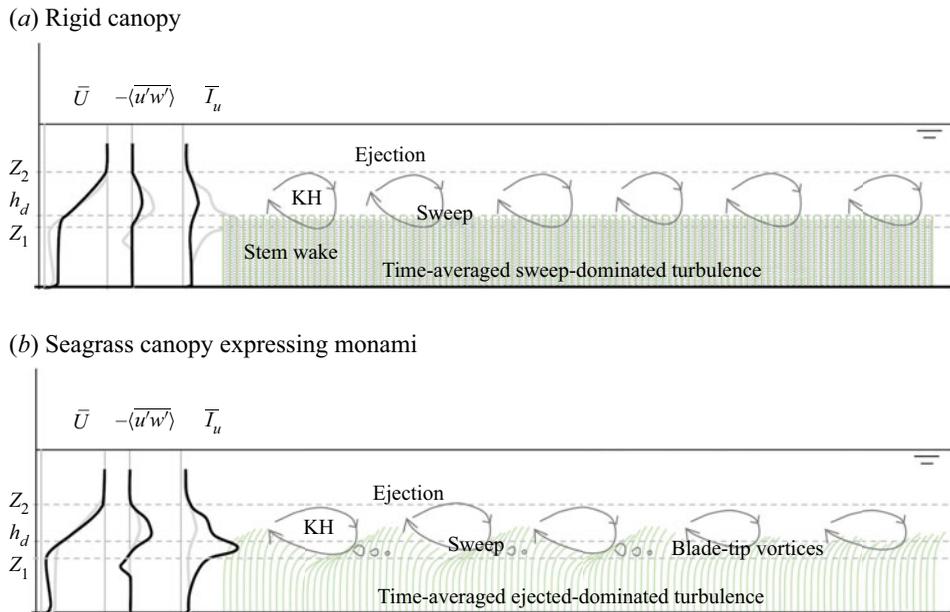
(*a*) Rigid canopy

(*b*) Seagrass canopy expressing monami

Figure 18. Schematic summary of flow processes associated with (*a*) rigid canopy and (*b*) flexible canopy based on $Re \sim 10^5$.

results and provided support for novel insights pointed out below. The novel methods enabled quantitative analysis of inner–outer canopy interactions using a combination of time–frequency (wavelet) and conditional phase-average, low-order (Fourier-based) tools. This is only possible with full optical access and high-frame-rate flow characterisation.

While previous research has identified the presence of turbulence frequencies consistent with KH vortices above seagrass canopies, our space–time analysis provides robust and compelling confirmation through visual and statistical analysis. Furthermore, through the use of instantaneous high-speed data, time–frequency analysis reveals that these coherent vortices may have a compact extent. This indicates that KH-like vortices are inconsistent or that their magnitude varies such that the Strouhal number associated with predictions is not entirely valid. The recognition of coherent vortex variability is of considerable importance when understanding seagrass system dynamics, specifically the mixing processes and turbulent fluxes if KH presence and magnitude are assumed constant. The states dominated by KH vortices express coherent waving and monami phenomenon in agreement with previous literature, although the canopy motion amplitude is reduced when coherent vortices are diminished. Furthermore, we show that the canopy underwent phases of highly coordinated deflected motions and phases of uncoordinated blade deflections, thus varying the exposed blade surface area.

The results support previous findings that canopy deflection inhibits the entrainment of canopy top sweeps into the lower canopy regions. Yet, we further uncover new dynamics within the canopy due to the canopy motion. Specifically, we present a hypothesis based on the SPOD modes on how the canopy motion modulates the interaction between above and within canopy flows and subsequently confirm through conditional averaging that the upward canopy motion results in a dominance of ejection events within the canopy. For the first time, the results reveal that the turbulence dynamics within flexible seagrass canopies

transitions from sweep to ejection as *Re* and *Ca* increases; this phenomenon is absent in rigid canopies.

The conceptual schematic illustrated in figure 18 embodies the common and distinct features of the flow in the seagrass and rigid canopies. The changes in turbulence process are critical to the lower canopy processes, including the potential bedload and suspended sediment dynamics. It is worth stressing that the distribution, or characteristic profiles, of the streamwise velocity component, kinematic shear stress and turbulence kinetic energy all exhibit different features in the two scenarios. The depth-restricted stresses in the seagrass reduce mixing and extend hydraulic retention, which are fundamental to biological processes, including nutrient and particulate exchange with the outer flow and providing greater bed protection (e.g. Christianen *et al.* 2013; Ondiviela *et al.* 2014; Guannel *et al.* 2015; Paul 2018; Paquier *et al.* 2019). These protective processes are not evident within the rigid canopy.

Author ORCIDs.

Shyuan Cheng https://orcid.org/0000-0001-8563-9054;

Leonardo P. Chamorro https://orcid.org/0000-0002-5199-424X.

REFERENCES

ABDOLAHPOUR, M., GHISALBERTI, M., MCMAHON, K. & LAVERY, P.S. 2018 The impact of flexibility on flow, turbulence, and vertical mixing in coastal canopies. *Limnol. Oceanogr.* **63** (6), 2777–2792.

ALBAYRAK, I., NIKORA, V., MILER, O. & O'HARE, M. 2012 Flow-plant interactions at a leaf scale: effects of leaf shape, serration, roughness and flexural rigidity. *Aquat. Sci.* **74** (2), 267–286.

BAI, K. & KATZ, J. 2014 On the refractive index of sodium iodide solutions for index matching in PIV. *Exp. Fluids* **55**, 4.

BAILEY, B.N. & STOLL, R. 2016 The creation and evolution of coherent structures in plant canopy flows and their role in turbulent transport. *J. Fluid Mech.* **789**, 425–460.

BLOIS, G., BRISTOW, N.R., KIM, T., BEST, J.L. & CHRISTENSEN, K.T. 2020 Novel environment enables PIV measurements of turbulent flow around and within complex topographies. *J. Hydrol. Engng* **146**, 5.

BLOIS, G., CHRISTENSEN, K.T., BEST, J.L., ELLIOTT, G., AUSTIN, J., DUTTON, J.C., BRAGG, M., GARCIA, M.H. & FOUKE, B.W. 2012 A versatile refractive-index-matched flow facility for studies of complex flow systems across scientific disciplines. *AIAA Paper* 2012-0736.

CAROPPI, G., VÄSTILÄ, K., JÄRVELÄ, J., ROWIŃSKI, P.M. & GIUGNI, M. 2019 Turbulence at water-vegetation interface in open channel flow: experiments with natural-like plants. *Adv. Water Resour.* **127**, 180–191.

CHEN, Z., JIANG, C. & NEPF, H. 2013 Flow adjustment at the leading edge of a submerged aquatic canopy. *Water Resour. Res.* **49** (9), 5537–5551.

CHRISTIANEN, M.J.A., VAN BELZEN, J., HERMAN, P.M.J., VAN KATWIJK, M.M., LAMERS, L.P.M., VAN LEENT, P.J.M. & BOUMA, T.J. 2013 Low-canopy seagrass beds still provide important coastal protection services. *PLoS ONE* **8**, 5.

CHUNG, H., MANDEL, T., ZARAMA, F. & KOSEFF, J.R. 2021 Local and nonlocal impacts of gaps on submerged canopy flow. *Water. Resour. Res.* **57** (2), e2019WR026915.

CLARKE, S.J. 2002 Vegetation growth in rivers: influences upon sediment and nutrient dynamics. *Prog. Phys. Geog.* **26** (2), 159–172.

COTTON, J.A., WHARTON, G., BASS, J.A.B., HEPPELL, C.M. & WOTTON, R.S. 2006 The effects of seasonal changes to in-stream vegetation cover on patterns of flow and accumulation of sediment. *Geomorphology* **77** (3–4), 320–334.

EDGAR, G.J. 1990 The influence of plant structure on the species richness, biomass and secondary production of macrofaunal assemblages associated with western australian seagrass beds. *J. Expl Mar. Biol. Ecol.* **137** (3), 251–240.

FALTER, J.L., ATKINSON, M.J., LOWE, R.J., MONISMITH, S.G. & KOSEFF, J.R. 2007 Effects of nonlocal turbulence on the mass transfer of dissolved species to reef corals. *Limnol. Oceanogr.* **52** (1), 274–285.

FINNIGAN, J.J., SHAW, R.H. & PATTON, E.G. 2009 Turbulence structure above a vegetation canopy. *J. Fluid Mech.* **637**, 387–424.

GAMBI, M.C., NOWELL, A.R. & JUMARS, P.A. 1990 Flume observations on flow dynamics in *Zostera marina* (eelgrass) beds. *Mar. Ecol. Prog. Ser.* **61**, 159–169.

GHISALBERTI, M. & NEPF, H. 2005 Mass transport in vegetated shear flows. *Environ. Fluid Mech.* **5** (6), 527–551.

GHISALBERTI, M. & NEPF, H. 2006 The structure of the shear layer in flows over rigid and flexible canopies. *Environ. Fluid Mech.* **6** (3), 277–301.

GHISALBERTI, M. & NEPF, H. 2009 Shallow flows over a permeable medium: the hydrodynamics of submerged aquatic canopies. *Transp. Porous Med.* **78** (3), 385–402.

GHISALBERTI, M. & NEPF, H.M. 2002 Mixing layers and coherent structures in vegetated aquatic flows. *J. Geophys. Res.* **107** (C2), 3011.

GHISALBERTI, M. & NEPF, H.M. 2004 The limited growth of vegetated shear layers. *Water Resour. Res.* **40**, 7.

GUANNEL, G., RUGGIERO, P., FARIES, J., ARKEMA, K., PINSKY, M., GELFENBAUM, G., GUERRY, A. & KIM, C.-K. 2015 Integrated modeling framework to quantify the coastal protection services supplied by vegetation. *J. Geophys. Res.: Oceans* **120** (1), 324–345.

HAMED, A.M., SADOWSKI, M.J., NEPF, H.M. & CHAMORRO, L.P. 2017 Impact of height heterogeneity on canopy turbulence. *J. Fluid Mech.* **813**, 1176–1196.

HO, C.-M. & HUERRE, P. 1984 Perturbed free shear layers. *Annu. Rev. Fluid Mech.* **16** (1), 365–422.

IKEDA, S. & KANAZAWA, M. 1996 Three-dimensional organized vortices above flexible water plant. *ASCE J. Hydraul. Engng* **122** (11), 634–640.

JIN, Y., KIM, J.-T., HONG, L. & CHAMORRO, L.P. 2018 Flow-induced oscillations of low-aspect-ratio flexible plates with various tip geometries. *Phys. Fluids* **30**, 9.

LIU, D., DIPLAS, P., FAIRBANKS, J.D. & HODGES, C.C. 2008 An experimental study of flow through rigid vegetation. *J. Geophys. Res.* **113** (F4), F04015.

LOWE, R.J., KOSEFF, J.R, MONISMITH, S.G. & FALTER, J.L. 2005 Oscillatory flow through submerged canopies: 2. Canopy mass transfer. *J. Geophys. Res.: Oceans* **110** (C10), C10017.

LUHAR, M. & NEPF, H.M. 2011 Flow-induced reconfiguration of buoyant and flexible aquatic vegetation. *Limnol. Oceanogr.* **56** (6), 2003–2017.

LUHAR, M. & NEPF, H.M. 2013 From the blade scale to the reach scale: a characterization of aquatic vegetative drag. *Adv. Water Resour.* **51**, 305–316.

LUHAR, M. & NEPF, H.M. 2016 Wave-induced dynamics of flexible blades. *J. Fluid Struct.* **61**, 20–41.

LUHAR, M., ROMINGER, J. & NEPF, H. 2008 Interaction between flow, transport and vegetation spatial structure. *Environ. Fluid Mech.* **8** (5-6), 423–439.

LUMLEY, J.L. 1970 Stochastic tools in turbulence. In *Applied Mathematics and Mechanics*, vol. 12. *Academic Press*.

MANDEL, T.L., GAKHAR, S., CHUNG, H., ROSENZWEIG, I. & KOSEFF, J.R. 2019 On the surface expression of a canopy-generated shear instability. *J. Fluid Mech.* **867**, 633–660.

MARJORIBANKS, T.I., HARDY, R.J., LANE, S.N. & PARSONS, D.R. 2017 Does the canopy mixing layer model apply to highly flexible aquatic vegetation? Insights from numerical modelling. *Environ. Fluid Mech.* **17** (2), 277–301.

NEPF, H. & GHISALBERTI, M. 2008 Flow and transport in channels with submerged vegetation. *Acta Geophys.* **56** (3), 753–777.

NEPF, H.M. 2012 Hydrodynamics of vegetated channels. *J. Hydraul. Res.* **50** (3), 262–279.

NEPF, H.M. & VIVONI, E.R. 2000 Flow structure in depth-limited, vegetated flow. *J. Geophys. Res.: Oceans* **105** (C12), 28547–28557.

NEZU, I. & SANJOU, M. 2008 Turbulence structure and coherent motion in vegetated canopy open-channel flows. *J. Hydro-Environ. Res.* **2** (2), 62–90.

NORBERG, C. 1994 An experimental investigation of the flow around a circular cylinder: influence of aspect ratio. *J. Fluid Mech.* **258**, 287–316.

O'CONNOR, J. & REVELL, A. 2019 Dynamic interactions of multiple wall-mounted flexible flaps. *J. Fluid Mech.* **870**, 189–216.

OKAMOTO, T., NEZU, I. & SANJOU, M. 2016 Flow–vegetation interactions: length-scale of the 'monami' phenomenon. *J. Hydraul. Res.* **54** (3), 251–262.

OKAMOTO, T.-A. & NEZU, I. 2009 Turbulence structure and 'monami' phenomena in flexible vegetated open-channel flows. *J. Hydraul. Res.* **47** (6), 798–810.

ONDIVIELA, B., LOSADA, I.J., LARA, J.L., MAZA, M., GALVÁN, C., BOUMA, T.J. & VAN BELZEN, J. 2014 The role of seagrasses in coastal protection in a changing climate. *Coast. Engng* **87**, 158–168.

PAQUIER, A.-E., MEULÉ, S., ANTHONY, E.J., LARROUDÉ, P. & BERNARD, G. 2019 Wind-induced hydrodynamic interactions with aquatic vegetation in a fetch-limited setting: implications for coastal sedimentation and protection. *Estuaries Coasts* **42** (3), 688–707.

PAUL, M. 2018 The protection of sandy shores – can we afford to ignore the contribution of seagrass? *Mar. Pollut. Bull.* **134**, 152–159.

POGGI, D., PORPORATO, A., RIDOLFI, L., ALBERTSON, J.D. & KATUL, G.G. 2004 The effect of vegetation density on canopy sub-layer turbulence. *Boundary-Layer Meteorol.* **111** (3), 565–587.

PRENTICE, C., HESSING-LEWIS, M., SANDERS-SMITH, R. & SALOMON, A.K. 2019 Reduced water motion enhances organic carbon stocks in temperate eelgrass meadows. *Limnol. Oceanogr.* **64**, 2389–2404.

DE LOS SANTOS, C.B., ONODA, Y., VERGARA, J.J., PÉREZ-LLORÉNS, J.L., BOUMA, T.J., LA NAFIE, Y.A., CAMBRIDGE, M.L. & BRUN, F.G. 2016 A comprehensive analysis of mechanical and morphological traits in temperate and tropical seagrass species. *Mar. Ecol. Prog. Ser.* **551**, 81–94.

SCHMIDT, O.T. & COLONIUS, T. 2020 Guide to spectral proper orthogonal decomposition. *AIAA J.* **58** (3), 1023–1033.

SCHMIDT, O.T., TOWNE, A., RIGAS, G., COLONIUS, T. & BRÈS, G.A. 2018 Spectral analysis of jet turbulence. *J. Fluid Mech.* **855**, 953–982.

SIEBER, M., PASCHEREIT, C.O. & OBERLEITHNER, K. 2016 Spectral proper orthogonal decomposition. *J. Fluid Mech.* **792**, 798–828.

TAIRA, K., BRUNTON, S.L., DAWSON, S.T.M., ROWLEY, C.W., COLONIUS, T., MCKEON, B.J., SCHMIDT, O.T., GORDEYEV, S., THEOFILIS, V. & UKEILEY, L.S. 2017 Modal analysis of fluid flows: an overview. *AIAA J.* **55** (12), 4013–4041.

TOWNE, A., SCHMIDT, O.T. & COLONIUS, T. 2018 Spectral proper orthogonal decomposition and its relationship to dynamic mode decomposition and resolvent analysis. *J. Fluid Mech.* **847**, 821–867.

TU, J.H., ROWLEY, C.W., LUCHTENBURG, D.M., BRUNTON, S.L. & KUTZ, J.N. 2014 On dynamic mode decomposition: theory and applications. *J. Comput. Dyn.* **1** (2), 391–421.

VACCHI, M., DE FALCO, G., SIMEONE, S., MONTEFALCONE, M., MORRI, C., FERRARI, M. & BIANCHI, C.N. 2017 Biogeomorphology of the mediterranean posidonia oceanica seagrass meadows. *Earth Surf. Process.* **42** (1), 42–54.

WAYCOTT, M., *et al.* 2009 Accelerating loss of seagrasses across the globe threatens coastal ecosystems. *Proc. Natl Acad. Sci. USA* **106** (30), 12377–12381.

WEITZMAN, J.S., AVENI-DEFORGE, K., KOSEFF, J.R. & THOMAS, F.I.M. 2013 Uptake of dissolved inorganic nitrogen by shallow seagrass communities exposed to wave-driven unsteady flow. *Mar. Ecol. Prog. Ser.* **475**, 65–83.

WEITZMAN, J.S., ZELLER, R.B., THOMAS, F.I.M. & KOSEFF, J.R. 2015 The attenuation of current- and wave-driven flow within submerged multispecific vegetative canopies. *Limnol. Oceanogr.* **60** (6), 1855–1874.

WILSON, C.A.M.E., STOESSER, T., BATES, P.D. & PINZEN, A.B. 2003 Open channel flow through different forms of submerged flexible vegetation. *ASCE J. Hydraul. Engng* **129** (11), 847–853.

YUE, W., MENEVEAU, C., PARLANGE, M.B., ZHU, W., VAN HOUT, R. & KATZ, J. 2007 A comparative quadrant analysis of turbulence in a plant canopy. *Water Resour. Res.* **43**, 5.

ZELLER, R., ZARAMA, F., WEITZMAN, J. & KOSEFF, J. 2014 Self-similarity of wakes in wave-driven canopy flow. In *American Physical Society Division of Fluid Dynamics Meeting Abstracts*, pp. R32–004.

ZHANG, Y., TANG, C. & NEPF, H. 2018 Turbulent kinetic energy in submerged model canopies under oscillatory flow. *Water Resour. Res.* **54** (3), 1734–1750.